

M2L TRANSLATION OPERATORS FOR KERNEL INDEPENDENT FAST MULTIPOLE METHODS ON MODERN ARCHITECTURES *

SRINATH KAILASA[†], TIMO BETCKE[‡], AND SARAH EL KAZDADI[§]

Abstract. Current and future trends in computer hardware, in which the disparity between available flops and memory bandwidth continues to grow, favour algorithm implementations which minimise data movement even at the cost of more flops. In this study we review the requirements for high performance implementations of the kernel independent Fast Multipole Method (kiFMM), a variant of the crucial FMM algorithm for the rapid evaluation of N -body potential problems. Performant implementations of the kiFMM typically rely on Fast Fourier Transforms for the crucial M2L (Multipole-to-Local) operation. However, in recent years for other FMM variants such as the black-box FMM also BLAS based M2L translation operators have become popular that rely on direct matrix compression techniques. In this paper we present algorithmic improvements for BLAS based M2L translation operator and benchmark them against FFT based M2L translation operators. In order to allow a fair comparison we have implemented our own high-performance kiFMM algorithm in Rust that performs competitively against other implementations, and allows us to flexibly switch between BLAS and FFT based translation operators.

Key words. FMM, High Performance Computing, M2L, Rust, multipole-to-local, kernel-independent FMM

MSC codes. 65-04, 65Y05, 65Y10, 65Y15, 65Y20

1. Introduction. The Fast Multipole Method (FMM) as originally presented by Greengard and Rokhlin [11] accelerates potential evaluation problems of the form

$$(1.1) \quad \phi(x_i) = \sum_{j=1}^N K(x_i, y_j) q(y_j), \quad i = 1, \dots, M$$

where the potential ϕ is evaluated at a set of target points, $\{x_i\}_{i=1}^M$, due to a set of densities, $\{q_j\}_{j=1}^N$, corresponding to a set of source points, $\{y_j\}_{j=1}^N$, and $K(\cdot, \cdot)$ is the interaction kernel. In cases where $K(\cdot, \cdot)$ is non-oscillatory and displays favourable properties the FMM enables the accelerated computation of (1.1) in just $\mathcal{O}(P(N + M))$, where P is a constant such that $P \ll M$, $P \ll N$ that controls the accuracy of the approximation. This is a significant algorithmic speed-up compared to naive direct $\mathcal{O}(NM)$ evaluation of (1.1).

The interaction kernel $K(\cdot, \cdot)$ naturally arises in science and engineering, for example the Laplace kernel, which describes electrostatic or gravitational interactions between sets of sources and targets is defined by

$$(1.2) \quad K(x, y) = \begin{cases} \frac{1}{2\pi} \log\left(\frac{1}{\|x-y\|}\right), & (2D) \\ \frac{1}{4\pi\|x-y\|}, & (3D) \end{cases}$$

The FMM rests on the intuition that potential evaluations between distant clusters of source and target points can be computed with a compressed representation

*Submitted to the editors August 15, 2024.

Funding: Srinath Kailasa is supported by EPSRC studentship 2417009, Timo Betcke is supported by EPSRC grants EP/W026260/1 and EP/W007460/1.

[†]Department of Mathematics, University College London, London, UK. (srinath.kailasa.18@ucl.ac.uk).

[‡]Department of Mathematics, University College London, London, UK (t.betcke@ucl.ac.uk)

[§](sarahelkazdadi@gmail.com)

of the potential due to the source cluster, leading to a reduction in the number of terms computed directly with the sum (1.1). However since its original formulation CPU architectures have evolved significantly, favouring algorithms that can map to the SIMD paradigm in which high performance is achieved by maximising data re-use per flop and distributing computations across multiple cores. In Table 2.1 we see that on commodity CPUs even with a naive direct implementation we can compute the interaction of one hundred thousand points in under a second (if carefully optimised for SIMD and memory caching). Details of the CPUs are given in Table B.3.

In this paper we focus on the kernel-independent FMM, a popular version of the Fast Multipole Method first introduced in [26]. In [17] the PVFMM code was described, which uses FFT based Multipole-to-Local (M2L) translation operators together with careful memory layouts and SIMD optimisations to achieve a high-performance implementation of the FMM on current generation CPU architectures. We will call this M2L variant FFT-M2L in the remainder of this paper. We summarise the method as implemented in our software in Appendix A.

In parallel to progress in the kiFMM black-box fast multipole methods were developed which are based on Chebyshev interpolation of kernels, see e.g. [9, 18]. These represent the M2L operation as direct matrix operation and use low-rank compression techniques to accelerate the M2L evaluation. In the following we simply call this variant of M2L translation BLAS-M2L.

The advantage of the BLAS-M2L is that it is algorithmically easier than the FFT-M2L and requires less involved memory reorderings to become efficient. However, it depends strongly on the low-rank compressibility of the M2L interactions, which makes this approach far more efficient for the FMM in two dimensions than in three dimensions. In this paper we investigate whether the BLAS-M2L can be competitive with respect to the FFT-M2L for the kiFMM in three dimensions for the Laplace kernel (1.2).

In order to provide a fair environment for comparison we have developed our own kiFMM implementation using Rust as a modern performant low-level language. Within our implementation via Rust traits different implementations of translation operators can be selected. We have made sure to carefully optimise the implementation to achieve similar levels of performance as PVFMM in order to have a good baseline for benchmarking.

The main contributions of this paper are as follows.

- A careful description of algorithmic improvements to speed-up BLAS based translation operators, improve cache re-use and maximise algorithmic intensity.
- Extensive benchmarking of the FFT-M2L vs the BLAS-M2L using our own kiFMM implementation for the Laplace kernel in three dimensions.

Modern CPU designs increasingly have specific registers to accelerate matrix-multiplication operations in the context of neural networks. It is therefore important to optimise classical computational algorithms to fully utilise BLAS3 based linear algebra operations as much as possible, and in this paper we give a realistic comparison of FFT-M2L and BLAS-M2L to demonstrate that the latter is competitive with FFT-M2L implementations on current hardware even for three-dimensional problems where interaction ranks between source and target boxes are significantly more challenging than in two space dimensions.

In Section 2 we review the basics of the kiFMM. Then in Section 3 we focus on BLAS based implementations of the M2L operator. We discuss data layout, compression techniques and implementational tricks to speed up the computation. We

provide single node benchmarks in Section 4, and a reflection on our results in Section 5.

1.1. Related Work. Though many past works have focussed on the optimisation of the field translation operation for analytical FMMs [13, 10, 7, 12, 8, 25], relatively few have focussed on the field translation operator as it appears in the kiFMM, which amounts to a series of dense matrix vector products in which the matrix is known to be numerically low rank. The original presentation by Ying et. al [26] reports that BLAS-M2L schemes using SVDs to compress the interaction matrices are unsatisfactory when tested on kernels in three dimensions, due to insufficient rank decay and high setup costs due to the SVD, instead recommending an FFT-M2L approach. The implementation of the FFT-M2L was optimised for CPUs in PVFMM [17], which is re-implemented by other modern kiFMM implementations such as ExaFMM [24]. Fong and Darve [9] reconsider a BLAS-M2L alongside SVD compression for the field translation operations for their black-box FMM based on Chebyshev interpolation for field approximation. This is extended by Messner et. al [18], who study optimal compression schemes to address the high setup costs, as well as blocking techniques for CPU based black-box FMM methods. These techniques are utilised in their implementation, ScalFMM [4]. Takahashi et. al. also developed an early GPU implementation based on similar techniques [22], however their study was limited to single precision problems. Despite past developments in fast field translations for algebraic FMMs, to the best of the authors' knowledge, there has been no direct comparison for three dimensional problems between the FFT-M2L implemented by current state of the art softwares [17, 24] and an highly optimised BLAS-M2L for modern processor architectures, though some work has been done for analytical FMMs [10]. Furthermore, the passage of time since these articles has seen the maturity high performance cross-platform open source BLAS libraries [23, 1], as well as platform specific implementations [19, 2], optimised for maximal cache-reuse and vector processing, making it important to reconsider BLAS-M2L schemes for field translation in the kiFMM.

2. Fast Multipole Method. The FMM relies on a degenerate approximation for the kernels, $K(.,.)$, such that (1.1) when evaluated between distant clusters of distant target, $\{x_i\}_{i=1}^M$, and source points, $\{y_j\}_{j=1}^N$, can be expressed as sum

$$(2.1) \quad \phi(x_i) \approx \sum_{p=1}^P \sum_{j=1}^N A_p(x_i) B_p(y_j) q(y_j), \quad i = 1, 2, \dots, M$$

where P , which we call the ‘expansion order’, is chosen such that $P \ll M, P \ll N$, and the functions A_p and B_p are determined by the particular approximation scheme of an FMM method. In the original presentation the calculation of

$$\hat{q}_p(y_j) = \sum_{j=1}^N B_p(y_j) q(y_j), \quad p = 1, 2, \dots, P$$

corresponded to the construction of analytical expansions of the kernel function representing the potential due to the source densities at the set of source points. The calculation

$$\phi(x_i) \approx \sum_{p=1}^P A_p(x_i) \hat{q}_p(y_j), \quad i = 1, 2, \dots, M$$

represents the evaluation of this potential at the set of target points.

The accuracy of the approximation (2.1) depends on a sufficient distance between clusters of sources and targets, referred to as *admissibility*. FMMs therefore split (1.1) for a given target cluster into *near* and *far* components

$$(2.2) \quad \phi(x_i) = \sum_{y_j \in \text{Near}(x_i)} K(x_i, y_j) q(y_j) + \sum_{y_j \in \text{Far}(x_i)} K(x_i, y_j) q(y_j),$$

the latter of which are taken to be admissible and can be approximated by (2.1) with the near component evaluated directly.

The FMM achieves its asymptotic complexity by partitioning the problem domain into a hierarchical data structure, commonly an octree in three dimensions or a quadtree in two dimensions, where a bounding box is placed over all sources and targets and recursively subdivided into equal sub-boxes, called its children. For a box B with side length d centred at c , we define its near field \mathcal{N}_B as all boxes that lie within a box of side length $3d$ centered at c , including B itself. Its far field \mathcal{F}_B is the complement of this. The idea is then to compress evaluation of interactions for each target box where a source box can be considered admissible, ie. in its far field, by using approximations to represent the field generated by far-field boxes. The approximations for potential due to a set of source densities are encoded using *multipole* and *local* expansions. Multipole expansions are used to describe potentials in the exterior of given box generated from sources in that box, and local expansions are used to describe potentials generated by a source in a box which is considered in the far field of a given box. The terms ‘multipole’ and ‘local’ are common terminology across methods derived from the FMM, even those which use an alternative approximation scheme. For octrees we refer to adjacent boxes, which share a face, edge, or vertex as *neighbours*, the eight child boxes of a given box, B , as *siblings*. Translations between these expansion representations are what gives the FMM its complexity, in particular,

- **multipole to multipole (M2M):** Translation of the multipole expansion of a child box to one centered on its parent box. This allows the accumulation of a multipole expansions representing child boxes as one traverses the tree from finest to coarsest level.
- **multipole to local (M2L):** Translation of the multipole expansion of a source box into a local expansion of a non adjacent target box whose parent is a neighbour of the source box’s parent. Such boxes for a given target box, B , are admissible and are referred to as its *interaction list*, I_B . In three dimensions $|I_B| \leq 189$.
- **local to local (L2L):** Translation of a local expansion of a parent box, to one centered on a child box. This allows the accumulation of a local expansion representing ancestor boxes as one traverses the tree from coarsest to finest level.

The algorithm for non-oscillatory kernels, based on *uniform refinement* such that all leaf boxes are of the same size, proceeds in a recursive two step procedure.

1. **Upward Pass:** First multipole expansions are encoded for boxes at the leaf level, in a ‘point to multipole’ (P2M) step. We then recurse by level, from finest to coarsest boxes, applying the M2M translation to each one.
2. **Downward Pass:** The tree is then traversed from coarsest to finest boxes, the local expansion is accumulated from both (i) a box’s parent (L2L) and (ii) source boxes in its interaction list (M2L). Specified in this way, the local expansion encodes the potential at a box B due to boxes in \mathcal{F}_B . At the

leaf level, the local expansion is evaluated at target points in each leaf box (L2P) and the potential due to adjacent boxes is calculated directly using (1.1) known as the point to point (P2P) operation.

We see that during the upward and downward passes, each target box interacts with a fixed number of source boxes. Indeed, an octree for a set of points N discretised such that each of leaf box contains a bounded number of points, results in $\sim N$ leaf boxes and depth $\log_8(N)$ contains $\mathcal{O}(N)$ boxes in total, giving a runtime complexity of $\mathcal{O}(\kappa N)$, where κ is a scalar constant that depends on the number of interactions for the M2L and P2P operations.

2.1. Performance Characteristics of the FMM. FMM performance is determined by the implementations of the M2L and P2P operations during the downward pass, which define the FMM's runtime. Broadly, the P2P operation is compute bound and is naturally expressed using either SIMD or SIMT paradigms as the evaluations per target are independent of each other. Choosing relatively smaller degrees of refinement for the hierarchical data structure results in a large near field calculations for each leaf box, which can be performed quickly for moderate problems sizes as we show in Table 2.1.

The M2L when implemented naively results in non-contiguous memory access patterns and resulting cache misses from having to index data corresponding to potentially discontinuous boxes in the hierarchical tree [6]. The fact that each box needs to perform up to 189 M2L translations in three dimensions leads the M2L operation to dominate runtime for deep trees. This trade-off between shallow trees and P2P bound implementations and deep trees with M2L bound implementations characterises the performance of the FMM.

We note that the performance of our P2P implementation alleviates the need for *adaptive refinement* of the hierarchical data structure, in which leaf boxes are refined until they contain fewer than a user-specified threshold of points. Previously adaptive FMMs have been recommended for highly non-uniform point distributions, and are used to limit the P2P operation by increasing the number of admissible source boxes which may ostensibly be in the near field of a target box as defined above but are refined to a greater extent and therefore amenable to compression. However, this approach requires additional interaction lists which must be calculated at runtime from the point data [26] as well as deeper trees to cope with the extreme point distributions. Ensuring contiguous data access is challenging when handling interaction lists, which as we see below introduces significant memory movement (see Section 3.2), and deeper trees make FMMs bound by the M2L implementation. Furthermore, adaptive implementations require additional global sorts of the tree's leaves in order to restrict the size of adjacent boxes, known as balancing, which limits the size of the resulting interaction lists. This can be a bottleneck in distributed implementations [20], and can be avoided by using a tree based on uniform refinement. In our implementation we instead use a weaker form of adaptivity, whereby branches which contain no point data are dropped from the final tree.

2.2. Kernel Independent Fast Multipole Method.

2.2.1. Forming Multipole and Local Expansions. We review the kiFMM of Ying. et. al [26], which makes use of the method of fundamental solutions for field approximations. Consider the construction of a ‘multipole’ expansion corresponding to a set of source densities in a box B , as in the left picture of Figure 2.1. We begin by constructing an ‘equivalent surface’, $y^{B,u}$, discretised by a set of evenly spaced points

Precision	Number of Points	Apple M1 Pro	AMD 3790X
Single Threaded			
Single	5,000	$12.7 \pm 0.2 \text{ (ms)}$	$10.9 \pm 0.2 \text{ (ms)}$
	20,000	$202.6 \pm 0.6 \text{ (ms)}$	$170.8 \pm 0.8 \text{ (ms)}$
Double	5,000	$30.6 \pm 0.1 \text{ (ms)}$	$24.6 \pm 0.1 \text{ (ms)}$
	20,000	$488 \pm 1 \text{ (ms)}$	$400 \pm 0.81 \text{ (ms)}$
Multi Threaded			
Single	20,000	$35.6 \pm 0.1 \text{ (ms)}$	$5.9 \pm 0.1 \text{ (ms)}$
	100,000	$865 \pm 10 \text{ (ms)}$	$148.3 \pm 0.2 \text{ (ms)}$
	500,000	$21.8 \pm 0.1 \text{ (s)}$	$3.84 \pm 0.2 \text{ (s)}$
Double	20,000	$82.8 \pm 0.5 \text{ (ms)}$	$12.3 \pm 0.5 \text{ (ms)}$
	100,000	$2.1 \pm 0.5 \text{ (s)}$	$307 \pm 0.8 \text{ (ms)}$
	500,000	$56.1 \pm 0.5 \text{ (s)}$	$10.9 \pm 0.1 \text{ (s)}$

Table 2.1: Runtimes for single and multi threaded direct $O(N^2)$ evaluation of (1.1) for the 3D Laplace kernel in our SIMD vectorised implementation, where we consider the source and target points to be the same set, with randomly assigned source densities.

with associated ‘equivalent densities’, $q^{B,u}$, with u signifying that we are talking about ‘upwards surfaces’ for the upward construction of multipole expansions. We match the field generated by these to that generated by the true source densities at a further enclosing ‘check surface’, $x^{B,u}$ that covers both B and $y^{B,u}$ to arrive at the equation

$$(2.3) \quad \int_{y^{B,u}} K(x, y) q^{B,u} = \sum_{i \in I_s^B} K(x, y_i) q_i = \phi^{B,u}(x), \quad x \in x^{B,u}$$

where $\phi^{B,u}$ is the (upward) ‘check potential’, and I_s^B is the index set of the sources contained in B , $\{y_i\}_{i \in I_s^B}$ and their associated densities, $\{q_i\}_{i \in I_s^B}$. Replacing the integral by a sum over the equispaced points that form the equivalent surface and evaluate at the target points in the check surface we obtain a matrix equation

$$(2.4) \quad Kq = \phi$$

with K an $N_{\text{check}} \times N_{\text{equiv}}$ matrix with entries $K(x_i, y_j)$ with $x_1, \dots, x_{N_{\text{check}}}$ the evaluation points on the check surface $x^{B,u}$ and $y_1, \dots, y_{N_{\text{equiv}}}$ the source points on the equivalent surface $y^{B,u}$, where N_{check} and N_{equiv} are the number of evaluation points on the check surface and source points on the equivalent surface respectively. Eq (2.4) defines an ill-conditioned least-squares problem. In [26] Ying et. al. proposed to solve this problem as a Tikhonov regularised normal equation of the form

$$(2.5) \quad q = (\alpha I + K^* K)^{-1} K^* \phi.$$

Here, α is a scalar regularisation parameter. Correspondingly one can construct local expansions using the surfaces as shown in the right figure of Figure 2.1, where now the check surface, $x^{B,d}$, must be enclosed by the equivalent surface, $y^{B,d}$. Here d in the index is used to signify that these are ‘downward’ surfaces.

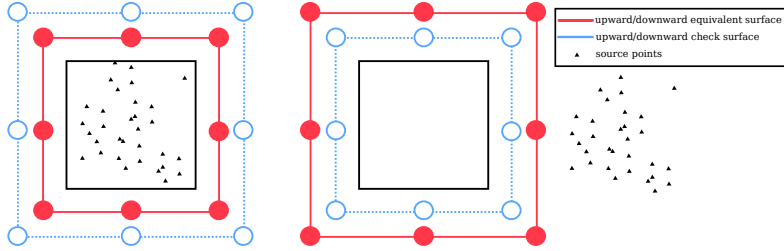


Fig. 2.1: We illustrate the equivalent/check surfaces and associated boxes in \mathbb{R}^3 , where we show a corresponding cross section. In the left picture we illustrate the situation in the ‘P2M’ operation, where we are trying to construct an approximation to the potential generated by points in a box by matching it to that generated by a set of equivalent density points placed on a fictitious surface enclosing it. In the right picture we illustrate the ‘P2L’ operation, where we are now trying to construct an approximation to the potential generated by points in a box’s far-field within the box. Adapted from Figure 4 in [26].

2.2.2. Translation Operators. The M2M, L2L and M2L operators are formed using the same technique as above, and are illustrated in Figure 2.2. For the M2M and L2L, forming the required surfaces, we match the field generated by the child/parent box’s equivalent densities at the parent/child box’s check surface respectively to find the check potential. This results in equations of the form of (2.5) for the calculation of the the multipole/local expansions, respectively.

We explicitly show the procedure for the M2L operator. The downward check potential, $\phi^{B,A,d}$, at the downward check surface of a target box B , $x^{B,d}$, due to a source box A in \mathcal{F}_B during a multipole to local field translation, shown in the right-most picture of Figure 2.2 is written as

$$(2.6) \quad \phi^{B,A,d}(x) = \int_{y^{B,d}} K(x, y) q^{B,A,d}(y) dy = \int_{y^{A,u}} K(x, y) q^{A,u}(y) dy, \text{ for all } x \in x^{B,d}$$

Represented as a matrix equation the calculation of $q^{B,A,d}$ is done using the check potential, $\phi^{B,A,d}$, that is the field values due to the expansion in box A evaluated at the check surface for B . With $\phi^{B,A,d} = K_{A,B} q^{A,u}$ the check potential generated from the equivalent sources in A , we need to match the equivalent sources in B by solving

$$(2.7) \quad K_B q^{B,A,d} = \phi^{B,A,d}$$

We again solve for the equivalent densities, corresponding to the local expansion, using Tikhonov regularisation to account for the ill-posed nature of the matrix equation, and arrive at

$$(2.8) \quad q^{B,A,d} = (\alpha I + K_B^* K_B)^{-1} K_{A,B} q^{A,u}$$

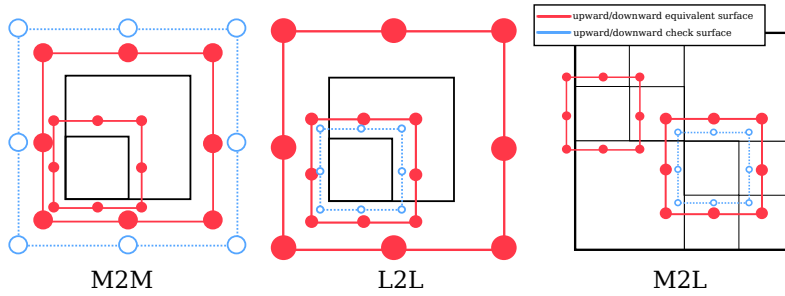
$$(2.9) \quad =: \tilde{K}_B^{-1} K_{A,B} q^{A,u}$$

$$(2.10) \quad = \tilde{K}_B^{-1} \phi^{B,A,d}.$$

We note that this operation needs to be done for all up to 189 boxes in the interaction list of B with the final equivalent potential from the M2L being given as $q^{B,d} = \sum_A q^{B,A,d} = \tilde{K}_B^{-1} \sum_A K_{A,B} q^{B,u}$.

The calculation of the check potential is a dense matrix-vector product, where $K_{A,B}$ is known to be low rank, and therefore amenable to numerical compression for example via the SVD. Alternatively, for kernels which are translation invariant such that $K(x, y) = K(x - y)$, by choosing the upward equivalent surfaces and downward check surfaces to be defined equivalently with respect to a given box, the evaluation of the check potential can be interpreted as a three dimensional convolution and can therefore be accelerated with fast Fourier transforms (FFT). We note that \tilde{K}_B^{-1} depends only on the downward equivalent and check surfaces of a box, if these are chosen to be the same relative to a given box, this can be cached and, depending on kernel properties, scaled at each level of the tree.

Fig. 2.2: As in Figure 2.1, we illustrate the translations as cross sections of the surfaces, which are cubes in \mathbb{R}^3 . Adapted from Figure 5 in [26].



In our BLAS-M2L implementation we optionally choose more check than equivalent points when creating surfaces, in order to create an overdetermined system to solve problems of the form (2.5). This can lead to greater accuracy in the final evaluated potential, with lower expansion orders and therefore fewer required flops [3]. We determine the exact number of check points heuristically for a given accuracy (Appendix B). We note that this isn't possible for the FFT-M2L, which requires the check and equivalent surfaces to be discretised to the same degree.

3. BLAS based M2L operators.

3.1. Compression and Application of M2L Matrices. In order to compress the numerically low rank matrices in (2.4) we build upon the ideas first presented in [9] and extended in [18] for the black-box FMM which uses Chebyshev interpolation matrices for translation operators. Starting by identifying the matrix in (2.4) with a transfer vector, which are used to describe the relative orientations between a target box and source boxes in its interaction list [18], as K_t , where $t \in T_l$ is the set of all unique transfer vectors at a level l . We assemble a single matrix row-wise

$$K_{\text{fat}} = [K_1 \quad \dots \quad K_{|T_l|}]$$

and column-wise

$$K_{\text{thin}} = \begin{bmatrix} K_1 \\ \dots \\ K_{|T_l|} \end{bmatrix}.$$

These larger matrices can be compressed with SVDs as rank k matrices, giving

$$(3.1) \quad K_{\text{fat}} \approx U\Sigma \begin{bmatrix} V_1^T & \dots & V_{|T_l|}^T \end{bmatrix} = U\Sigma \tilde{V}^T,$$

$$(3.2) \quad K_{\text{thin}} \approx \begin{bmatrix} R_1 \\ \dots \\ R_{|T_l|} \end{bmatrix} \Lambda S^T = \tilde{R} \Lambda S^T,$$

where U and S are unitary matrices. U is of size $N_{\text{check}} \times k$, and S is of size $N_{\text{equiv}} \times k$ and k is chosen such that the cut-off rank corresponds to a desired accuracy ϵ in the final evaluated potential.

From [9], considering each element of K_{fat} and K_{thin} corresponding to a given $t \in T_l$, using that S has orthonormal columns we insert $S^T S = I$ into (3.2)

$$\begin{aligned} K_t &= R_t \Lambda S^T \\ &= R_t \Lambda S^T S S^T \\ &= [R_t \Lambda S^T] S S^T \\ &= K_t S S^T \\ &= U \Sigma V_t^T S S^T \end{aligned}$$

Using also that U has orthonormal columns we insert $U^T U = I$ into the above to obtain

$$\begin{aligned} K_t &= U U^T U \Sigma V_t^T S S^T \\ &= U [U^T U \Sigma V_t^T S] S^T \\ &= U [U^T K_t S] S^T \end{aligned}$$

Giving,

$$(3.3) \quad K_t = U C_t S^T,$$

where

$$C_t = U^T K_t S$$

is of size $k \times k$, which we call the *compressed M2L matrix*, which operates on the *compressed multipole expansion*

$$\tilde{q} = S^T q$$

and returns the *compressed check potential*

$$\tilde{\phi} = C_t S^T q = C_t \tilde{q}.$$

Examining the errors obtained in the singular values of K_{fat} and K_{thin} for the three dimensional Laplace kernel one observes that once can express K_{fat} and K_{thin} with a rank of $k \sim N/2$ [9]. Pre-processing to find the compressed multipole expansions, $\tilde{q} = S^T q$ requires $\mathcal{O}(kN_{\text{equiv}})$ flops per source box. Similarly post-processing to recover the check potentials $\phi = U \tilde{\phi}$, which requires $\mathcal{O}(kN_{\text{check}})$ per target box.

For translational invariant and homogeneous kernels which are also symmetric such that $K_{\text{fat}} = K_{\text{thin}}^T$ where the check and equivalent surfaces are discretised to the same degree, we can compute a single SVD. Without homogeneity an SVD would have to be computed level-wise for each set of associated matrices, resulting in level-wise U and S , and without symmetry or equivalent check and equivalent surface discretisation we need two SVDs per level. We note that the Laplace kernel is homogeneous, translation invariant and symmetric, and that $|T_l| = 316$ [18]. This can be seen by considering the interactions of a given box and its siblings together. Each sibling box's near field interactions correspond to $27 = 3^3$ transfer vectors, including with itself. For a given sibling box, its far field interactions correspond to $189 = 6^3 - 3^3$ transfer vectors, where 6^3 comes from the fact that the interaction list of each box is defined from non-adjacent children of a box's parent. Similarly, the union of all unique transfer vectors for a set of siblings is 7^3 , accounting for the transfer vectors corresponding to near field interactions gives a total of $316 = 7^3 - 3^3$. This corresponds to $|T_l|$, and represents the largest number of transfer vectors per level for such kernels.

As the value of k in this formulation is dictated by the highest-rank interaction in T_l , the cost of applying most C_t can be lowered with another SVD for each individual K_t , $t \in T_l$, such that

$$(3.4) \quad C_t = \bar{U}_t \bar{\Sigma}_t \bar{V}_t^T = \bar{U}_t \bar{V}'_t^T$$

where \bar{U}_t and \bar{V}'_t are of size $k \times k_t$, $\bar{\Sigma}$ is of size $k_t \times k_t$, and k_t can be chosen to preserve ϵ [18]. In order to determine k and k_t we use a user specified threshold, using a grid search to determine the optimal parameter for a given accuracy (Appendix B).

The combination of a global compression over all $t \in T_l$ and a directional compression for each $t \in T_l$ reduces the application cost of the matrices for computing the check potential via BLAS operations. The ranks k and k_t found by this compression determine the size of the matrix vector products, and are determined by the kernel.

Past BLAS-M2L schemes, as in [18], use kernel symmetry and translation invariance to convert (2.4) from a matrix vector product calculating the check potential between each source and target box pair, into a matrix multiplication where multiple check potentials are computed at once between source boxes in a target box's interaction list which share a transfer vector. Further blocking is done across siblings and their respective interaction lists.

In our implementation we notice we can identify *all* source and target boxes at each level in the downward pass that share a transfer vector, not just across shared transfer vectors between a single target box's interaction list, or multiple sibling boxes. With this we can compute all check potentials for target boxes with at most $|T_l|$ BLAS level 3 calls at tree level l appropriately accumulating the check potentials for each target box. High performance is enabled with this approach by the powerful blocking techniques available in modern BLAS implementations [23, 1, 2, 19], which are able to optimally tile large matrix multiplications and apply optimisations such as loop re-ordering, tiling and SIMD vectorisations with minimal configuration. We note that the number of flops required by this method is greater than for an FFT-M2L scheme, however the greater memory re-use per flop in comparison to the low arithmetic intensity Hadamard product required during FFT-M2L leads to the highly competitive overall runtimes we observe in our benchmarks.

Computing the SVDs required by our scheme is costly in comparison to the FFTs required for the FFT-M2L, especially for high expansion orders in double precision.

We accelerate this pre-computation using the randomised SVD (rSVD) [14] to compute the large SVDs required of K_{fat} and/or K_{thin} , in contrast to the deterministic SVDs used in the past [18]. We only consider ‘one shot’ rSVDs, that avoid slow power iterations which repeatedly apply the QR decomposition to compute the orthonormal basis of the subspace into which the matrix is projected, and instead use only oversampling and knowledge of the kernel properties to improve the performance of the rSVD. Specifically, we use the result that K_{fat} and K_{thin} are of rank $k \sim N/2$ for the Laplace kernel as found in [9], and compute the rSVD with this rank estimate. We provide the the optimal oversampling parameters found for K_{fat} and K_{thin} for the Laplace kernel in Appendix B to achieve a desired accuracy in the final evaluated potentials via the FMM.

We note that the SVDs required during the directional compression step (3.4) are not so onerous due to the smaller matrix sizes in comparison to K_{fat} and K_{thin} . We therefore use deterministic SVD here while retaining reasonable setup times as we show in Table 4.2. We note that the cost of the required deterministic QR decomposition required by the rSVD remains significant for higher multipole expansion orders in double precision.

3.1.1. Algorithm. Our approach for evaluating the check potentials for each target box at each level l during the downward pass is then,

1. Identify N_s source boxes at level l associated with each transfer vector $t \in T_l$, where T_l are the unique transfer vectors associated with level l and $N_s < N_{\text{source}}$ if they appear in an interaction list of target boxes at this level, where N_{source} source boxes are associated with multipole data at level l .
2. Compute the compressed multipole expansions from the multipole expansions, q_i , of each of N_{source} , using a single level 3 BLAS call.

$$[\tilde{q}_1, \dots, \tilde{q}_{N_{\text{source}}}] = S^T [q_1, \dots, q_{N_{\text{source}}}]$$

3. Compute the compressed check potentials in a loop over each $t \in T_l$, resulting in up to $|T_l|$ level 3 BLAS calls, each of the form

$$[\tilde{\phi}_1, \dots, \tilde{\phi}_{N_s}] = C_t [\tilde{q}_1, \dots, \tilde{q}_{N_s}]$$

Each $\tilde{\phi}_i$ is associated with a source box at level l i.e. contained in an interaction list of any target box at this level. These are accumulated in a buffer containing N_{target} compressed check potentials associated with each target box at level l .

$$[\tilde{\phi}_1, \dots, \tilde{\phi}_{N_{\text{target}}}]$$

4. Compute the check potential at each of N_{target} target boxes at level l using another level 3 BLAS call.

$$[\phi_1, \dots, \phi_{N_{\text{target}}}] = U [\tilde{\phi}_1, \dots, \tilde{\phi}_{N_{\text{target}}}]$$

The entire scheme for computing the check potentials at each tree level l during the downward pass, consists of up to $|T_l| + 2$ level 3 BLAS calls per level, which for the Laplace kernel results in 318 calls per level [18]. We note that the permutation scheme in [18] could be used to further reduce the number of BLAS calls by blocking again by transfer vectors that differ only by orientation, however we find in practice that this is offset by the requirement of additional memory movements to form the required permutations.

Importantly, this approach allows us to easily compute the FMM for *multiple sets of source densities* sharing a set of target and source points, common in the application of FMMs to boundary integral equations. We simply identify all common translations corresponding to each right hand side of (1.1) at a given level, and pass them through the level 3 BLAS operation, letting the underlying BLAS library handle the required blocking for this larger calculation.

3.2. Data Access. For indexing the tree we rely on standard Morton encodings [21], which encode information about the spatial locality of boxes and allow us to store and look up associated multipole, local or potential data using an index pointer technique contiguously over sets of siblings, or adjacent sets of siblings. Being able to look up sets of sibling multipole and local data allows us to express the M2M and L2L operations as level 3 BLAS operations, further blocked over multiple sets of siblings at a given level.

For our BLAS-M2L method, we calculate the required translations as a pre-processing step. We process each box containing target points, level by level, identifying the source boxes associated with them via their interaction lists. We store each source, target pair box in a hashmap indexed by their corresponding transfer vector. During the loop over transfer vectors in the algorithm in Section (3.1.1) we allocate new buffers containing the source data to be translated and for storing the check potentials calculated via a multithreaded BLAS level 3 call. This ensures contiguous data structures for the BLAS call. We write the computed check potentials to a global buffer containing the check potentials associated with each target box, stored in Morton order, by using a buffer of mutable references corresponding to the check potentials of each target box at this level.

If a particular CPU has a large number of cores we find better performance by distributing the loop over transfer vectors in the algorithm of Section (3.1.1) across multiple threads, computing each BLAS level 3 call in a single thread. In this instance, we must wrap the mutable references for each target box’s check potential in a mutex in order to prevent a race condition. Additionally, in this case we set the number of threads used in the BLAS call to one to avoid thread oversubscription between the matrix multiplication and the multithreading across transfer vectors.

We perform the P2P operation in a parallel loop over each target leaf box, computing (1.1) in single threaded mode with respect to source coordinates, and associated densities, in each target box’s near field. Each set of coordinate triples are stored contiguously for each box in Morton order making it possible to use index pointers to create mappings between the Morton keys of source and target leaf boxes and associated coordinate data. A similar strategy is also used for source densities and potential data associated with each box, enabling an $\mathcal{O}(1)$ lookup cost for these data for each box.

4. Benchmarks. For a box with side length d , we took the inner and outer surfaces required by the kiFMM to have side length $1.05d$ and $1.95d$ respectively, as in [17, 24], which were found heuristically. We note that Apple’s Accelerate BLAS library used in benchmarks for the M1 Pro makes use of the specialised AMX registers for matrix computations available in recent Apple CPUs. In Tables 2.1, 4.1 and 4.2 we compute benchmarks with Rust’s Criterion library, which repeats experiments until the variance between samples is minimised from which we report the standard deviation as uncertainty to the nearest millisecond.

In Table 4.1 we report the mean observed end-to-end benchmark runtimes, as well as the M2L and P2P operator runtimes, for achieving a given relative error when

Table 4.1: Mean end-to-end (T_{FMM}), excluding setup times, M2L (T_{M2L}) and P2P (T_{P2P}) runtimes in milliseconds for achieving a given relative error (ϵ) with both BLAS-M2L and FFT-M2L when computing the Laplace potential for 1×10^6 uniformly distributed source and target points assigned random source densities. We report runtimes for the best parameter settings documented in Appendix B. For BLAS based field translations we also report the runtime per source density vector, when the FMM is called multiple times with different source density data for the same source/target point data. The number of source density vectors is given in brackets, and we highlight the fastest mean runtime per FMM call for each relative error.

(a) M1 Pro													
ϵ	BLAS (1)			BLAS (5)			BLAS (10)			FFT			T_{P2P}
	T_{FMM}	T_{M2L}	T_{P2P}	T_{FMM}	T_{M2L}	T_{P2P}	T_{FMM}	T_{M2L}	T_{P2P}	T_{FMM}	T_{M2L}	T_{P2P}	
Single Precision													
10^{-4}	223 \pm 3	113 \pm 3	95 \pm 1	207 \pm 1	84 \pm 1	110 \pm 1	199 \pm 1	79 \pm 4	120 \pm 1	172 \pm 3	64 \pm 1	95 \pm 1	
10^{-5}	255 \pm 3	137 \pm 3	96 \pm 2	245 \pm 5	116 \pm 1	111 \pm 2	231 \pm 1	106 \pm 1	110 \pm 1	278 \pm 5	160 \pm 4	96 \pm 2	
Double Precision													
10^{-7}	941 \pm 7	629 \pm 6	217 \pm 1	902 \pm 1	568 \pm 1	226 \pm 2	1068 \pm 4	691 \pm 3	234 \pm 1	1231 \pm 4	911 \pm 7	216 \pm 1	
10^{-9}	1690 \pm 12	107 \pm 1	1441 \pm 1	1771 \pm 6	123 \pm 2	1450 \pm 1	1759 \pm 4	118 \pm 1	1522 \pm 8	1891 \pm 13	275 \pm 12	1441 \pm 1	
10^{-11}	1925 \pm 15	222 \pm 2	1442 \pm 3	1990 \pm 3	234 \pm 1	1514 \pm 3	1953 \pm 3	229 \pm 1	1520 \pm 5	2262 \pm 35	536 \pm 2	1439 \pm 13	
(b) AMD 3790X													
ϵ	BLAS (1)			BLAS (5)			BLAS (10)			FFT			T_{P2P}
	T_{FMM}	T_{M2L}	T_{P2P}	T_{FMM}	T_{M2L}	T_{P2P}	T_{FMM}	T_{M2L}	T_{P2P}	T_{FMM}	T_{M2L}	T_{P2P}	
Single Precision													
10^{-4}	109 \pm 1	17 \pm 1	93 \pm 1	107 \pm 1	5 \pm 1	95 \pm 1	106 \pm 1	6 \pm 1	95 \pm 1	105 \pm 1	11 \pm 1	92 \pm 1	
10^{-5}	120 \pm 1	21 \pm 1	93 \pm 1	130 \pm 1	26 \pm 1	95 \pm 1	138 \pm 1	34 \pm 1	94 \pm 1	136 \pm 1	39 \pm 1	93 \pm 1	
Double Precision													
10^{-7}	273 \pm 1	74 \pm 1	183 \pm 1	347 \pm 1	134 \pm 2	183 \pm 1	353 \pm 1	148 \pm 1	183 \pm 1	437 \pm 5	220 \pm 1	182 \pm 1	
10^{-9}	398 \pm 1	186 \pm 1	183 \pm 1	501 \pm 1	336 \pm 1	183 \pm 1	515 \pm 1	352 \pm 1	182 \pm 1	685 \pm 5	459 \pm 1	182 \pm 1	
10^{-11}	762 \pm 2	517 \pm 1	182 \pm 1	919 \pm 1	638 \pm 1	183 \pm 1	938 \pm 1	683 \pm 1	183 \pm 1	1157 \pm 6	900 \pm 5	182 \pm 1	

computing the Laplace potential (1.1) for 1×10^6 uniformly distributed source and target points assigned random densities in three dimensions with both BLAS and FFT based field translations. Relative errors are reported from the mean relative error, computed against the direct evaluation of potentials for target points contained in a single leaf box with respect to all source points. The parameters corresponding to the best performance for a given relative error are reported for each hardware tested in Appendix B and found with a grid search.

On both architectures tested we observe that BLAS-M2L and FFT-M2L result in broadly similar end-to-end runtimes. The edge for the BLAS-M2L on the AMD architecture likely due to the optimal caching provided by the underlying BLAS library in contrast to the manual techniques used in the implementation of FFT-M2L (Appendix A). On the M1 Pro, the relatively large cache sizes and high memory transfer speeds are reflected in the increased performance per FMM call in single precision when using BLAS-M2L for FMMs called over multiple sets of source densities. This is no longer true in double precision on the M1 Pro and both single and double precision on the AMD architecture, likely the result of increased cache invalidations with the larger data sizes.

Our implementation heavily relies on simplified access patterns due to uniform octrees in which the only adaptivity is pruning empty branches. In Figure 4.1 we ex-

Table 4.2: Mean setup times in milliseconds for computing the required FFTs and Randomised SVDs for the benchmark problems in Table 4.1, ie. for computing the data required for FMMs to evaluate the potentials to a given accuracy given by the relative error ϵ . We use the BLAS and LAPACK versions in Table B.3 for each target.

ϵ	M1 Pro		AMD 3790X	
	rSVD	FFT	rSVD	FFT
Single Precision				
10^{-4}	681 ± 38	840 ± 9	75 ± 1	539 ± 1
10^{-5}	689 ± 34	908 ± 25	380 ± 1	569 ± 3
Double Precision				
10^{-7}	1180 ± 51	1155 ± 23	1079 ± 1	844 ± 1
10^{-9}	2037 ± 4	1280 ± 20	6313 ± 24	1469 ± 24
10^{-11}	11193 ± 337	2360 ± 71	30243 ± 22	2862 ± 83

amine the efficacy of our ‘weakly adaptive’ approach for computing the FMM with the Laplace kernel over a highly non-uniform point distribution. We observe a moderate increase in runtime, $\sim 50\%$, in comparison to an experiment over an equivalent number of uniformly distributed points, showing that for most applications this approach is sufficient over a fully adaptive FMM with its additional complexity.

5. Conclusion. In this paper we have shown that with suitable blocking and careful use of randomised SVDs a BLAS based kiFMM can be competitive with an FFT based kiFMM implementation. The advantage of the former is not only that the implementation itself is simpler, but also that BLAS operations are more and more accelerated by special CPU register extensions in modern CPUs. It also naturally extends itself to porting to batched BLAS implementations on GPUs, though latency and memory copy operations need to be carefully tuned for here. BLAS M2L operators also naturally extend to treating many FMM charges at the same time, giving potential for additional cache reuse.

The main trade-off is the relatively longer pre-computation time required due to its reliance on an SVD, and more sources of error in the evaluated potential as a result, due to the sensitivity of this compression on the properties of the kernel being evaluated. Given that emerging hardware architectures, both CPU and GPU, are likely to contain significant software and hardware optimisations for BLAS operations the importance of developing algorithm implementations which take advantage of this development will continue to grow.

Acknowledgments. We are grateful to Matthew Scroggs for his valuable assistance in software development during this research.

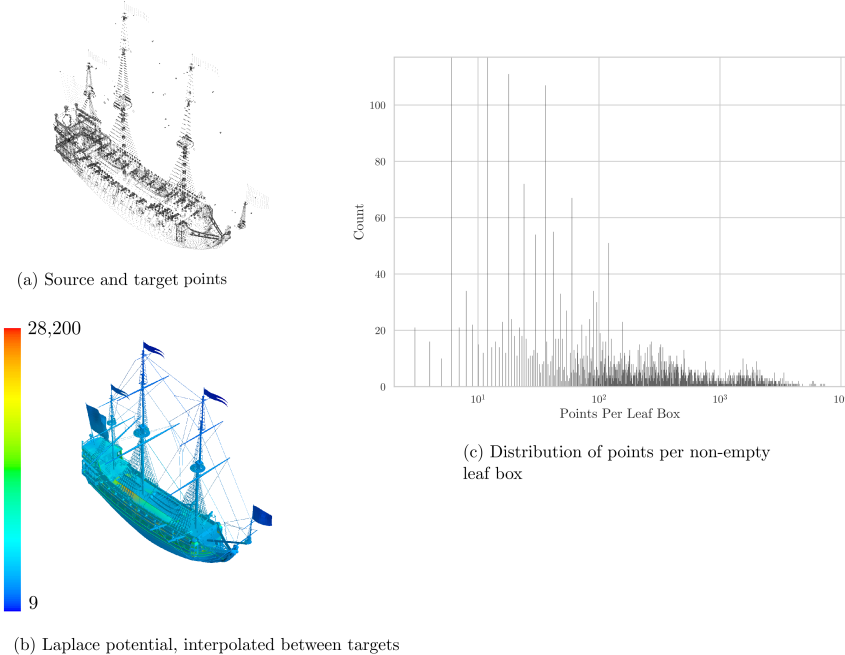


Fig. 4.1: The three dimensional Laplace potential (1.1) computed to relative error $\epsilon = 10^{-11}$ using BLAS-M2L with parameters as in Table 4.1 for this accuracy. The experiment is run on a highly-non uniform point distribution consisting of the 1,441,572 vertices of 480,524 triangles each with a random source density using a uniformly refined octree, refined to a depth of 5, containing 8192 non-empty leaf boxes. Here we take the source and target points to be the same set. The mean runtime was found to be 2.36 ± 0.01 s where we report over a 100 runs with standard deviation as an uncertainty on the AMD architecture in Table B.3. Computing the potential for an equivalent number of uniformly distributed source/target points we find the mean runtime to be 1.62 ± 0.01 s with octrees of depth 4, which we can take to be a baseline level of performance, implying that the non-uniformity resulted in an approximately 45 % greater runtime. The histogram illustrates the highly non-uniform point distribution, with leaf boxes containing anywhere between 1 and 10^4 points. The mesh is provided by [5].

Appendix A. FFT accelerated M2L.

We review the method introduced in [17] and re-implemented in [24] for maximising the arithmetic intensity of the evaluation of check potentials (2.4) using FFTs below. We use the case of a one dimensional problem for clarity.

For an order P multipole or local expansion, we described a check or equivalent surface as consisting of P evenly spaced points along each axis as shown in Figure 2.1 in three dimensions. In one dimension, this would correspond to a line shown in Figure A.2. We define the convolution grid as an embedding of this surface into a grid defined by $\tilde{P} = 2P$ points along each axis through its volume, that encloses the grid describing the equivalent surface (surface grid) and is aligned at a given corner of the surface grid. In three dimensions the convolution grid is instead a cube evenly discretised by \tilde{P} points along each axis. We thus note that the convolution grid consists of \tilde{P}^d points in dimension d . We define a sequence of kernel evaluations as

$$K_j = K(x_c, \tilde{y}_j),$$

where x_c is a chosen point on the target check surface and \tilde{y}_j are points on the convolution grid as shown in Figure A.2. This sequence captures all the unique kernel evaluations between the points discretising the source and target boxes. In the case of Figure A.2, we choose $x_c = x_0$ and construct a sequence

$$K[j] = \begin{cases} K(x_c, \tilde{y}_{j+1}), & j = 0, \dots, 2P-2 \\ 0, & j = 2P-1, \end{cases}$$

where we use zero padding to handle the circular shift. We also define a sequence of densities on the convolution grid, defined through our embedding of the surface grid, placing zeros where densities from the surface grid are not mapped,

$$\tilde{q}[j] = \begin{cases} 0, & j = 0, 1 \dots P-1, \\ q[j-P], & j = P, \dots, 2P-1, \end{cases}$$

where $q[i]$, $i = 0, \dots, P-1$, is the original sequence of densities on the surface grid.

We compute the check potential as a convolution of the flipped sequence $K'[2P-1-i] = K[i]$ with the source densities placed on the convolution grid

$$\phi[i] = \sum_{j=0}^{2P-1} \tilde{q}[j] K'[(i-j)_{2P}]$$

where $\phi[i]$ is the potential at $\phi(x_i)$.

Computed for a given box B , finding the check potential consists of mapping the sequence of densities to the convolution grid corresponding to the multipole expansions for each box A in its interaction list I_B , computing the DFT of this sequence and computing the Hadamard product with the result with the DFT of the flipped sequence of kernel evaluations corresponding to that particular relative position between source and target box which can potentially be precomputed and cached. The DFTs are accelerated with the FFT, however the component wise Hadamard product

is of low arithmetic intensity as each item of both sequence is used once per each required read and write operations.

In three dimensions, this is an $O(\tilde{P}^3)$ operation which requires $O(\tilde{P}^3)$ memory accesses. For this case the authors of [17] improve the arithmetic intensity by considering the interaction of 8 source siblings with 8 target siblings, allowing for efficient vectorisation. 8 siblings together are referred to as a ‘cluster’. All the M2L translations for a target cluster will occur with boxes that are children of the neighbours of the cluster’s shared parent, termed *source clusters*. We illustrate this in two dimensions in Figure A.1. In two dimensions the source clusters form a halo consisting of eight clusters, around each target cluster. In three dimensions this halo consists of 26 source clusters. In two dimensions, there are 16 unique interaction pairs of source and target boxes between a given source cluster and a target cluster, correspondingly in three dimensions there are 64 such interactions. Thus each source and target cluster will have a 64 corresponding sequences of Fourier coefficients of kernel evaluations $K^{(i)}[]$ of length $\hat{P} = \tilde{P}^3$, where i indexes the interaction between a source and target box contained in the source/target clusters being considered

$$\begin{aligned} [K^{(1)}, K^{(2)}, \dots, K^{(64)}] = \\ [[K^{(1)}[0], K^{(1)}[1], \dots, K^{(1)}[\hat{P} - 1]], \\ [K^{(2)}[0], K^{(2)}[1], \dots, K^{(2)}[\hat{P} - 1]], \\ \dots, \\ [K^{(64)}[0], K^{(64)}[1], \dots, K^{(64)}[\hat{P} - 1]]], \end{aligned}$$

corresponding to 64 unique relative positions between the source and target boxes contained in these clusters. These sequences are permuted into *frequency order*,

$$\begin{aligned} (A.1) \quad & [[K^{(1)}[0], K^{(2)}[0], \dots, K^{(64)}[0]], \\ & [K^{(1)}[1], K^{(2)}[1], \dots, K^{(64)}[1]], \\ & \dots, \\ & [K^{(1)}[\hat{P} - 1], K^{(2)}[\hat{P} - 1], \dots, K^{(64)}[\hat{P} - 1]]] \end{aligned}$$

The Fourier coefficients \hat{q} of the multipoles are ordered similarly. The Hadamard computation is then executed in blocks of 8×8 small Hadamard products between all source boxes in an 8-cluster with the corresponding target boxes in an 8-cluster. This allows for efficient vectorisation and cache re-use. Together with parallelisation across frequencies this approach achieves high throughput. With this strategy around typically around 10% of computations are redundant as not all relative positions of source clusters may exist for a given target cluster. In this case the corresponding sequence of Fourier transformed kernel evaluations is replaced with zeros.

Depending on the properties of the kernel, we can pre-compute and potentially scale the matrices corresponding to (A.1) for all 26 relative positions between source and target clusters in three dimensions at each level l . Additionally, for sequences of kernel evaluations that correspond to real numbers, such as for (1.2), the size of the resulting sequence of Fourier coefficients can be halved.

In order to further improve runtime performance, the original authors use explicit SIMD intrinsics for x86 architectures for the implementation of the 8×8 matrix

S_1^1	S_2^1	S_1^2	S_2^2	S_1^3	S_2^3
S_3^1	S_4^1	S_3^2	S_4^2	S_3^3	S_4^3
S_1^8	S_2^8	T_1	T_2	S_1^4	S_2^4
S_3^8	S_4^8	T_3	T_4	S_3^4	S_4^4
S_1^7	S_2^7	S_1^6	S_2^6	S_1^5	S_2^5
S_3^7	S_4^7	S_3^6	S_4^6	S_3^5	S_4^5

The source clusters (S_j^i) where i is the index of the source cluster and j is the index of each source box within a source cluster, for a target cluster (T_j) where j is the index of each target box within the target cluster.

Fig. A.1: Source and target clusters illustrated in two dimensions. Here a target cluster consisting of 4 sibling quadrants is shown in orange, and the eight source clusters, which consist of the target cluster’s parent’s neighbours are shown in blue.

vector product during the calculation in the parallel loop, as the sizes are too small to justify a BLAS call and autovectorisers struggle to optimise the complex multiply add operations required on x86. In our implementation we follow the recommendations of the Intel architecture reference for this operation for AVX and AVX2 instruction sets [15]. For Arm architectures, we use NEON FCMA instructions, which contain special intrinsics for performing fused complex multiply and add operations. Our software also contains a generic autovectorised implementation, allowing our codes to run on common hardware targets supported by Rust’s LLVM based compiler.

The frequency re-ordering together with reformulation as small efficient 8×8 Hadamard products is key to make the method compute bound. However, the permutations required to form and handle the frequency ordering results in practice in a complex code structure and care needs to be taken to do the re-ordering efficiently for it not to dominate execution time. In [17] this was achieved by re-ordering mutable references to the actual data. Access to mutable references by parallel threads is considered an anti-pattern in Rust, and despite being possible is not well supported due to the potential for race conditions and other parallel data access errors. Instead in our implementation we allocate new buffers to store the re-ordered data, which we can then iterate over in chunks corresponding to each frequency, and post-process the frequency ordered results for check potential back into Morton order. We note that there exists an emerging library for threadsafe parallel indirect access patterns in Rust, however we have not yet experimented with this [16].

As with our BLAS-M2L, the most challenging part of data access is ensuring the lookups required during the M2L for each box’s interaction list, I_B , are contiguous. The multipole data in the halo of each target box is stored in a single contiguous buffer, in Morton order, over the source boxes at a given level. For each target box, we calculate its halo, and use a technique of index pointers to look up required data, whereby we store together the index position of the start of each multipole/local data for a given box within the global buffer storing all multipole/local data with its associated Morton key. Using index pointers, we create references to the multipole data of each target box’s halo stored in frequency order. Therefore in the parallel loop we must lookup each reference in a loop over the halo data, and accumulate in a global buffer containing the check potentials for all target boxes, stored in frequency order and Morton order, un-permuting the check potentials from frequency order as

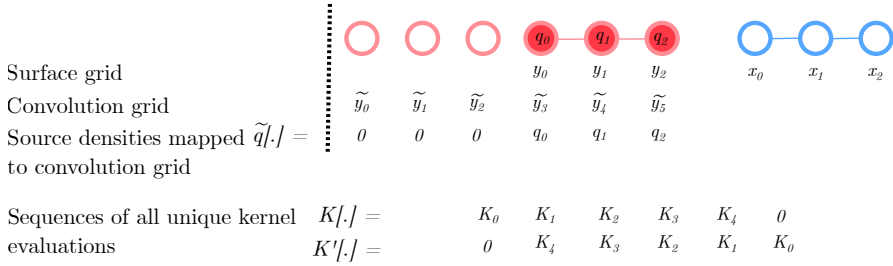


Fig. A.2: We show a one dimensional M2L translation for $p = 3$ expansions from the red source box $\{y_j\}_{j=0}^2$, embedded in a convolution grid $\{\tilde{y}_j\}_{j=0}^{2P-1}$, with associated multipole expansion coefficients $\{q_j\}_{j=0}^2$ to a blue target box $\{x_i\}_{i=0}^2$. We associate the required sequences of kernel evaluations $K[.]$, and the flipped sequence $K'[.]$, and the sequence of source densities $\tilde{q}[.]$ associated with points on the convolution grid

a post-processing step. Similarly to our BLAS-M2L approach, the halo of each target box is calculated as a pre-processing step, and removes the need to explicitly construct and process interaction lists by indexing the octree at runtime. Efficient cache usage is achieved in this method by processing the halos of multiple target clusters at once for each frequency.

Appendix B. Hardware and Software Parameters.

Here we document the optimal parameters that minimise FMM end-to-end runtimes found using a grid search for our software for both BLAS and FFT based field translations for evaluating (1.1) for the Laplace kernel (1.2) over a million uniformly distributed source and target points in order to achieve the mean relative errors ϵ reported for the benchmark experiments in Table 4.1, which are reported with respect to direct computation of potentials for target particles in a given leaf box. For FMMs computed with BLAS based M2L we show in Table B.1 the tree depth, d , equivalent surface order, P_e , check surface order, P_e , the number of oversamples in the ‘one shot’ randomised SVD, N_{over} , as well as the threshold used to cutoff singular values during the compression step, σ_{\min} . Similarly for FMMs computed with FFT based M2L In Table B.2 we show the tree depth, d , equivalent surface order (which is the same as the check surface order for this method), P_e , and block sizes of the number of target clusters when used when processing multiple target clusters during the parallel loop over frequencies, B . For the P2M operation which involves a BLAS level 3 call to form the check potential we use a block size of up to 4 sets of siblings, similarly for the M2M and L2L we use a block size of up to 2 sets of siblings in each BLAS level 3 call for check potential. This was found heuristically for the architectures tested.

Table B.1: Grid Search BLAS-M2L

ϵ	d	P_e	P_c	N_{over}	σ_{min}
Apple M1 Pro					
10^{-4}	5	3	3	5	1×10^{-7}
10^{-5}	5	3	4	5	1×10^{-4}
10^{-7}	5	6	6	10	1×10^{-6}
10^{-9}	4	7	8	20	1×10^{-6}
10^{-11}	4	9	11	10	1×10^{-6}
AMD 3790X					
10^{-4}	4	3	3	10	1×10^{-7}
10^{-5}	4	5	7	5	1×10^{-2}
10^{-7}	4	6	6	5	1×10^{-6}
10^{-9}	4	7	8	20	1×10^{-6}
10^{-11}	4	9	11	5	1×10^{-6}

Table B.2: Grid Search FFT-M2L

ϵ	d	P_e	B
Apple M1 Pro			
10^{-4}	5	3	256
10^{-5}	5	4	128
10^{-7}	5	6	128
10^{-9}	4	8	128
10^{-11}	4	10	64
AMD 3790X			
10^{-4}	4	3	32
10^{-5}	4	4	16
10^{-7}	4	6	32
10^{-9}	4	8	32
10^{-11}	4	10	32

Table B.3: Hardware and software used in our benchmarks, for the Apple M1 Pro we report only the specifications of its ‘performance’ CPU cores. We report per core cache sizes for L1/L2 and total cache size for L3. We note that the Apple M series of processors are designed with unusually large cache sizes, as well as unified memory architectures enabling rapid data access across specialised hardware units such as the performance CPU cores and the specialised matrix coprocessor used for BLAS operations when run with Apple’s Accelerate framework [2].

	Apple M1 Pro	AMD 3790X
Cache Line Size	128 B	64 B
L1i/L1d	192/128 KB	32/32 KB
L2	12 MB	512 KB
L3	24 MB	134 MB
Memory	16 GB	252 GB
Max Clock Speed	3.2 GHz	3.7 GHz
Sockets/Cores/Threads	1/8/8	1/32/64
Architecture	ArmV8.5	x86
SIMD Extensions	Neon	SSE, SSE2, AVX, AVX2
BLAS	Apple Accelerate	Open BLAS
LAPACK	Apple Accelerate	Open BLAS
FFT	FFTW	FFTW
Threading	Rayon	Rayon

REFERENCES

- [1] *OpenBLAS: An optimized BLAS library*, 2024, <https://www.openblas.net/>. Accessed: 2024-06-13.
- [2] APPLE INCORPORATED, *Accelerate Framework*, 2024, <https://developer.apple.com/documentation/accelerate>. Accessed: 2024-06-13.
- [3] A. H. BARNETT AND T. BETCKE, *Stability and convergence of the method of fundamental solutions for helmholtz problems on analytic domains*, Journal of Computational Physics, 227 (2008), pp. 7003–7026.
- [4] P. BLANCHARD, B. BRAMAS, O. COULAUD, E. DARVE, L. DUPUY, A. ETCHEVERRY, AND G. SYLVAND, *Scalfmm: A generic parallel fast multipole library*, in SIAM Conference on Computational Science and Engineering (SIAM CSE 2015), 2015.
- [5] BOLBOT, *Old ship*. Thingiverse, 2018, <https://www.thingiverse.com/thing:3253610>. Accessed: 2024-07-10.
- [6] A. CHANDRAMOLISHWARANY, K. MADDURI, AND R. VUDUC, *Diagnosis, tuning, and redesign for multicore performance: A case study of the fast multipole method*, in SC’10: Proceedings of the 2010 ACM/IEEE International Conference for High Performance Computing, Networking, Storage and Analysis, IEEE, 2010, pp. 1–12.
- [7] W. DEHNEN, *A hierarchical $o(n)$ force calculation algorithm*, Journal of Computational Physics, 179 (2002), pp. 27–42.
- [8] W. D. ELLIOTT AND J. A. BOARD, JR, *Fast fourier transform accelerated fast multipole algorithm*, SIAM Journal on Scientific Computing, 17 (1996), pp. 398–415.
- [9] W. FONG AND E. DARVE, *The black-box fast multipole method*, Journal of Computational Physics, 228 (2009), pp. 8712–8725.
- [10] P. FORTIN, *Multipole-to-local operator in the Fast Multipole Method: comparison of FFT, rotations and BLAS improvements*, PhD thesis, INRIA, 2005.
- [11] L. GREENGARD AND V. ROKHLIN, *A fast algorithm for particle simulations*, Journal of computational physics, 73 (1987), pp. 325–348.
- [12] L. GREENGARD AND V. ROKHLIN, *A new version of the fast multipole method for the laplace equation in three dimensions*, Acta numerica, 6 (1997), pp. 229–269.
- [13] N. A. GUMEROV AND R. DURAISWAMI, *Fast multipole methods on graphics processors*, Journal of Computational Physics, 227 (2008), pp. 8290–8313.
- [14] N. HALKO, P.-G. MARTINSSON, AND J. A. TROPP, *Finding structure with randomness: Probabilistic algorithms for constructing approximate matrix decompositions*, SIAM review, 53 (2011), pp. 217–288.
- [15] INTEL CORPORATION, *Intel 64 and IA-32 Architectures Optimization Reference Manual, Volume 1*, 2023, <https://www.intel.com/content/www/us/en/content-details/671488/intel-64-and-ia-32-architectures-optimization-reference-manual-volume-1.html>. Version 049, Last updated: September 5, 2023.
- [16] A. LONGVA, *paradis: Parallel processing with disjoint indices in rust*. <https://github.com/Andlon/paradis>, 2024.
- [17] D. MALHOTRA AND G. BIROS, *Pvfmm: A parallel kernel independent fmm for particle and volume potentials*, Communications in Computational Physics, 18 (2015), pp. 808–830.
- [18] M. MESSNER, B. BRAMAS, O. COULAUD, AND E. DARVE, *Optimized m2l kernels for the chebyshev interpolation based fast multipole method*, arXiv preprint arXiv:1210.7292, (2012).
- [19] NVIDIA CORPORATION, *cuBLAS Library Documentation*, 2024, <https://docs.nvidia.com/cuda/cUBLAS/index.html>. Accessed: 2024-01-29.
- [20] H. SUNDAR, D. MALHOTRA, AND G. BIROS, *Hyksort: a new variant of hypercube quicksort on distributed memory architectures*, in Proceedings of the 27th international ACM conference on international conference on supercomputing, 2013, pp. 293–302.
- [21] H. SUNDAR, R. S. SAMPATH, AND G. BIROS, *Bottom-up construction and 2: 1 balance refinement of linear octrees in parallel*, SIAM Journal on Scientific Computing, 30 (2008), pp. 2675–2708.
- [22] T. TAKAHASHI, C. CECKA, W. FONG, AND E. DARVE, *Optimizing the multipole-to-local operator in the fast multipole method for graphical processing units*, International Journal for Numerical Methods in Engineering, 89 (2012), pp. 105–133.
- [23] F. G. VAN ZEE AND R. A. VAN DE GEIJN, *Blis: A framework for rapidly instantiating blas functionality*, ACM Transactions on Mathematical Software (TOMS), 41 (2015), pp. 1–33.
- [24] T. WANG, R. YOKOTA, AND L. A. BARBA, *Exafmm: a high-performance fast multipole method library with c++ and python interfaces*, Journal of Open Source Software, 6 (2021), p. 3145.
- [25] C. A. WHITE AND M. HEAD-GORDON, *Rotating around the quartic angular momentum barrier in fast multipole method calculations*, The Journal of Chemical Physics, 105 (1996),

pp. 5061–5067.

[26] L. YING, G. BIROS, AND D. ZORIN, *A kernel-independent adaptive fast multipole algorithm in two and three dimensions*, Journal of Computational Physics, 196 (2004), pp. 591–626.